*Geophys. J. R. astr. Soc.* (1972) **27**, 57–80.

# Generalized Ray Theory for a Layered Sphere

**Freeman Gilbert and Donald V. Helmberger***

(Received 1971 August 2)†



*Summary*

Pulse propagation in a layered sphere can be investigated, in an approximate way, by what has come to be known as Cagniard's method. Classical methods are used in the analysis through the application of the Debye ray expansion. At this stage Lamb's observation, that the eikonal is linear in the frequency, is employed to bypass the usual methods for evaluation of the inverse transform integrals. The transient response for each Debye ray is obtained directly. It is estimated that the method can be applied to mantle $S$ pulses with periods less than 75 s, and to mantle $P$ pulses with periods less than 40 s. Preliminary results on lateral heterogeneity beneath North America are presented.

## Extension of generalized ray theory to spherical layers

The application of generalized ray theory to stratified media has been limited by the requirements that the stratification must be represented by homogeneous layers, and that the interfaces must be plane-parallel. When these two requirements are met, one uses plane-wave reflection and transmission coefficients and time delays to build up the solution to the problem (Weyl 1919; Pekeris 1948; Spencer 1960).

In the Cagniard–de Hoop method the time delay, $t$, ray parameter, $p$, velocity, $v$, and horizontal distance, $R$, are related by the classical formula

$$t = pR + \int^{z} (v^{-2} - p^2)^{\frac{1}{2}}\, dz. \tag{1}$$

In geometrical ray theory the ray parameter is constant along a ray and has the value

$$p = p_i = \sin i/v \tag{2}$$

where $i$ is the angle of incidence. The expression (1) for $t$ is stationary for $p = p_i$. In generalized ray theory the r.h.s. of (1) is the exponent in a complex integral with respect to $p$. Then $p_i$ is a saddlepoint and $t(p_i)$ is the arrival time of the pulse represented by the complex integral. Along the path of steepest descent from the saddlepoint the r.h.s. of (1) is real, because it is real at $p_i$, and increasing. Thus $t$ parametrizes the path of steepest descent $p(t)$ which allows the Cagniard inversion to be performed. The synthetic seismogram corresponding to a particular geometrical ray is represented by a function $f(p)$ evaluated on $p(t)$.

* Now at: Seismological Laboratory, Division of Geological Sciences, California Institute of Technology, Pasadena, California 91109.

† Received in original form 1970 October 29.

Generalized ray theory has not been used to study teleseismic phenomena because the sphericity of the level surfaces of velocity, $v$, and density, $\rho$, must be considered. However, it has been shown by Scholte (1956) and others that, for short pulses, the saddle-point method gives a result where *plane-wave* reflection and transmission coefficients appear.

It is natural to use this result in an attempt to apply the Cagniard–de Hoop method, in an approximate way, to spherical layers. In a sphere the classical ray parameter is $\gamma = r \sin i/v$ and Scholte (1956) has shown that a reflection coefficient $R(p)$ for plane layers is replaced by $R(\gamma/r)$ for spherical layers. In addition, for a sphere (1) becomes

$$t = \gamma\theta + \int^{r} (v^{-2} - \gamma^2 r^{-2})^{\frac{1}{2}}\, dr. \tag{3}$$

To convert (3) to (1) we replace $\gamma/r$ by $p$ and $\gamma\theta$ by $pR$. The horizontal distance $R$ is identified as the distance $r\theta$. For short pulses, the problem of constructing a generalized ray theory appears to offer no conceptual difficulties. We begin with the plane layer theory. The ray parameter, $p$, for plane layers is replaced by $\gamma/r$; the horizontal range $R$ is replaced by $r\theta$; geometrical spreading is taken into account by the factor $(\theta/\sin\theta)^{\frac{1}{2}}$; and the same reflection and transmission coefficients are used.

For example, suppose the Laplace transformed response $\bar{u}$ for the ray path shown in Fig. 1 is given by

$$\bar{u} = \frac{1}{\pi i} \int_{\Gamma} K_0(spR)\, \mathscr{F}(p)\, T_{32}(p)\, R_{21}(p)\, T_{23}(p) \exp(-s\psi)\, dp \tag{4}$$

where $\Gamma$ is the initial path from $p = -i\infty$ to $p = +i\infty$ and where

$$\psi = 2[(v_3^{-2} - p^2)^{\frac{1}{2}}(z_3 - z_2) + (v_2^{-2} - p^2)^{\frac{1}{2}}(z_2 - z_1)].$$

Then the approximation to $\bar{u}$, for short pulses, for the ray path shown in Fig. 2 is

$$\bar{u} = \frac{1}{\pi i} \left(\frac{\theta}{\sin\theta}\right)^{\frac{1}{2}} \int_{\Gamma} K_0(s\gamma\theta)\, \mathscr{F}(\gamma/a)\, T_{32}(\gamma/r_2)\, R_{21}(\gamma/r_1)\, T_{23}(\gamma/r_2) \exp(-s\psi)\, d\gamma\, a^{-1} \tag{5}$$

where

$$\psi = 2\left[\int_{r_1}^{r_2} (v_2^{-2} - \gamma^2/r^2)^{\frac{1}{2}}\, dr + \int_{r_2}^{a} (v_3^{-2} - \gamma^2/r^2)^{\frac{1}{2}}\, dr\right].$$

In both (4) and (5) $\mathscr{F}$ is the combined source and receiver directivity function,

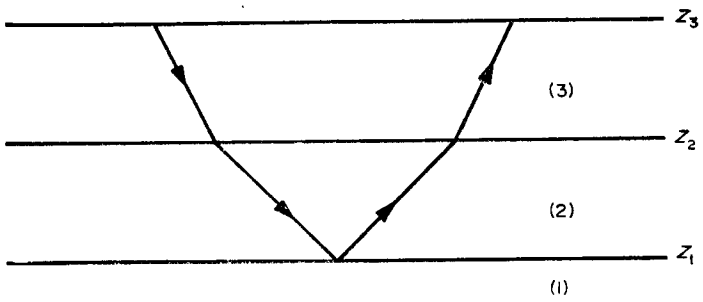


FIG. 1. Schematic diagram of the ray path that corresponds to the integral in equation (4).

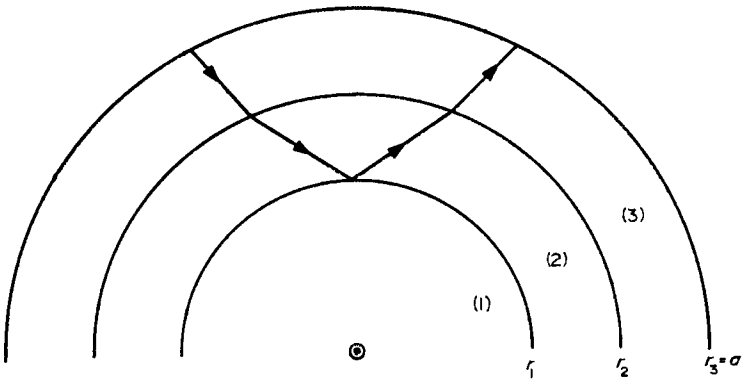


FIG. 2. Schematic diagram of the ray path that corresponds to the integral in equation (5).

assumed to be homogeneous in $p$. The Laplace inversion of (4) and (5) is discussed in Appendix B.

For a wide reflection, beyond the critical angle, the precursive head wave appears to travel along the *curved* interface, or refraction horizon. Another ray, a straight line, or chord, just below the interface, has been neglected in our approximation. In the limit, as the radius of the sphere approaches infinity, but layer thicknesses and horizontal distance, $a\theta$, are preserved, our approximate result approaches the exact result for plane layers. The contribution from the chord ray vanishes. Our approximation is asymptotic in reciprocal fractional powers of $ka$, and, in this respect, large $ka$ can arise either from large $a$ or large $s$. Consequently, since the contribution from the chord ray vanishes as $a \to \infty$, it vanishes as $s \to \infty$ and represents a 'blunter' pulse than the head wave. The contribution from the chord ray is always neglected in our approximations.

In principle, there is no more difficulty in evaluating (5) than (4) by the Cagniard–de Hoop method. In Appendix A we present the problem of the reflection of an *SH* pulse by a sphere to illustrate that (5) is, indeed, the correct approximation to the solution for short pulses. The question of determining the region of validity for the approximation is a difficult one and we have no quantitative answer. However, the work of Nussenzweig (1965) and others shows that not only $ka = 2\pi a/vT$ but also $(ka)^{\frac{1}{2}}$ must be large. For certain diffraction phenomena (e.g. the rainbow effect) even $(ka)^{\frac{1}{2}}$ must be large. In an expression $x \gg 1$ it is never clear whether $x > 10$ or $x > 100$, or some other figure is adequate. In scattering and diffraction problems $x > 3$ is frequently sufficient (Keller 1957, 58). If we take $(ka)^{\frac{1}{2}} \geqslant 3$ we have $ka \geqslant 30$. Taking $a = 3000$ km and $v = 8\ \mathrm{km\,s^{-1}}$ (for $S$ waves) we have

$$\frac{6a}{vT} \geqslant 30 \quad \text{or} \quad \frac{18000}{240} \geqslant T$$

so $S$ pulses in the mantle with periods less than 75 s could reasonably be expected to be well represented by expressions such as (5). For $P$ pulses we take $v = 15\ \mathrm{km\,s^{-1}}$ and find $T \leqslant 40$ s.

Thus we have some qualitative justification to expect that our approximate generalized ray theory is valid for mantle $P$ pulses shorter than 40 s and for mantle $S$ pulses shorter than 75 s.

As an initial application of our theory we shall calculate the theoretical seismograms for some recently proposed models of the upper mantle.

## Synthetic seismograms for the upper mantle

In recent years several velocity profiles have been proposed for the upper mantle. (We arbitrarily restrict our attention to depth less than 800 km.) Although the proposed models vary considerably, they can be classified into two types: those that have abrupt changes in velocity and those that are relatively smooth. The former have travel-time triplications and are favoured by Julian & Anderson (1968) and Johnson (1967). The latter are, in a sense, traditional models.

We investigate different models by computing synthetic seismograms, using generalized ray theory, and comparing them with observations. This use of amplitude information as an additional criterion in model making should decrease our uncertainty about the structure of the upper mantle. For the present we present results of studying NTS events.

A map of recording sites used in this study is given in Fig. 3. The observations are the short period vertical responses to the various NTS events. A profile of observations running NE, from the AARDVARK event, is given in Fig. 4. The four letter station code is given to the left of each seismogram. A similar plot running SE composed from a number of events is given in Fig. 5. The travel times of the first arrival for the two profiles are similar but the locations and amplitudes of later arrivals appear to be quite different. This discordant behaviour reflects lateral changes in the upper mantle. With the use of generalized ray theory we hope to elicit the nature of these lateral variations.

Using information derived from LRSM recordings of the type given in Figs 4 and 5, Julian & Anderson (1968) were able to produce a velocity profile that agrees with both first and second arrival times. Two simplified profiles containing the most prominent features are given in Fig. 6 as models B and C. In addition, a traditional model, model A, is given. It is based on a smooth upper mantle model taken from Dowling & Nuttli (1964).

In Fig. 6 only the $P$ velocity is shown. The $S$ velocity is obtained by multiplying the $P$ velocity of each model by Gutenberg's $S$ to $P$ velocity ratio. The density profile is the same for all three models and is based on the standard Bullen Model A.

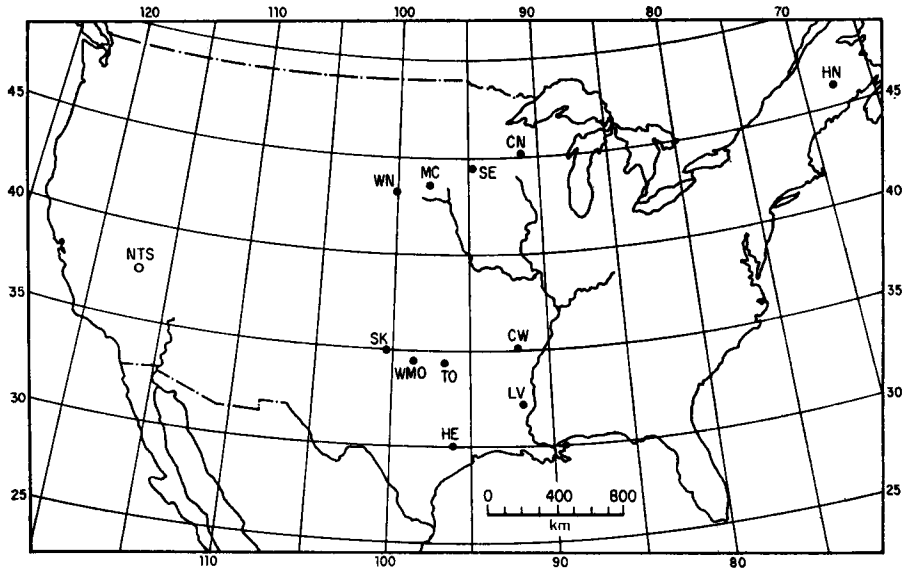


FIG. 3. Location of LRSM stations and Nevada Test Site (NTS).

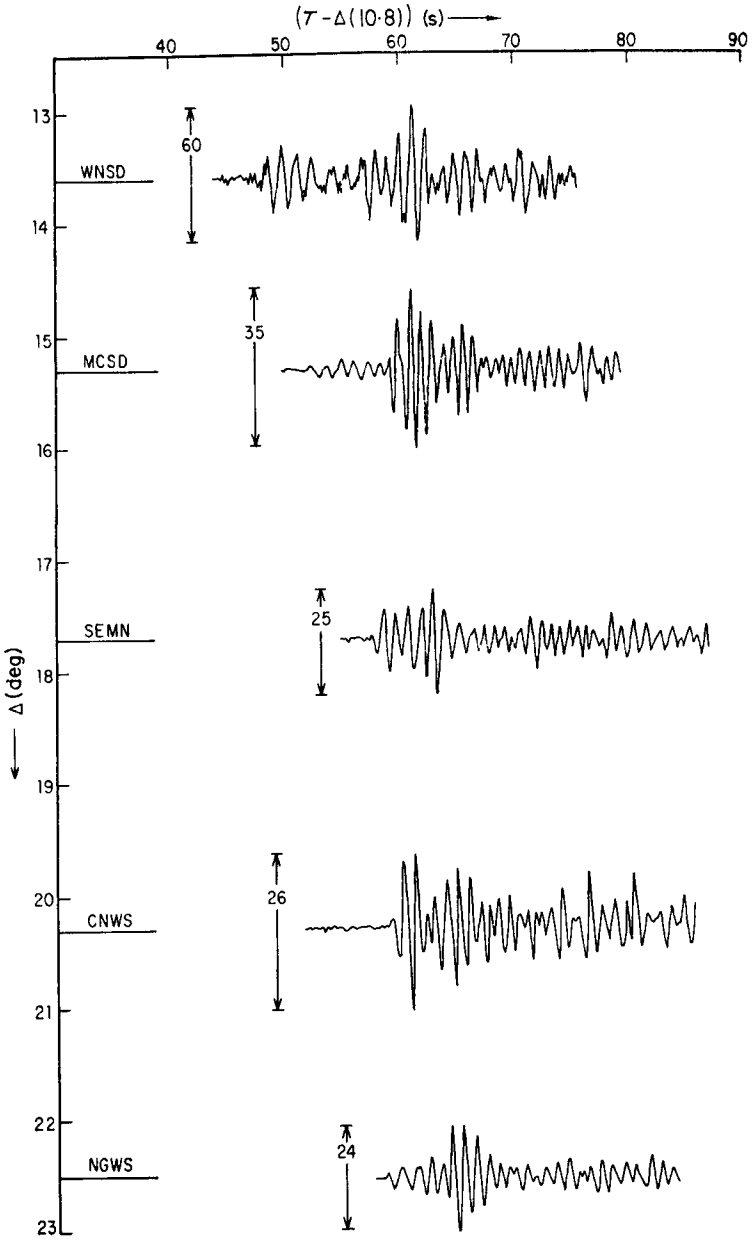


FIG. 4. NE record section for the AARDVARK event.

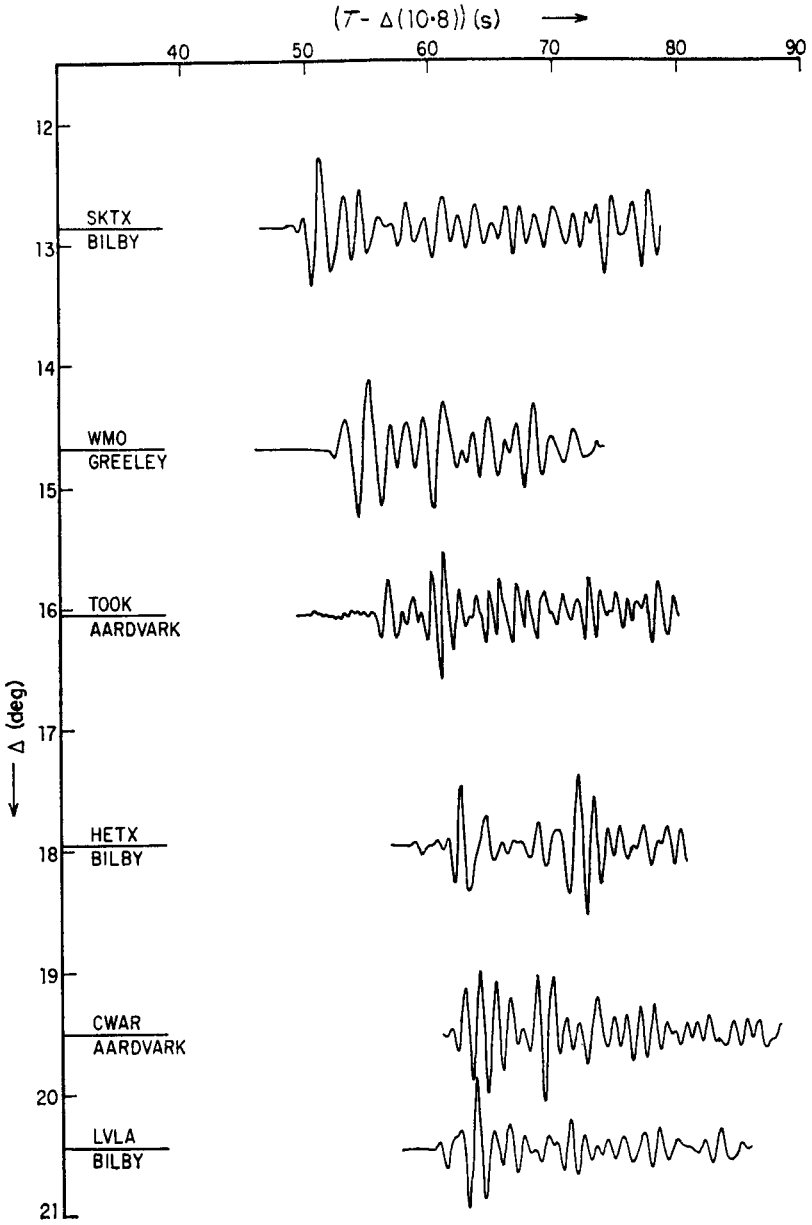


FIG. 5. SE composite record section.

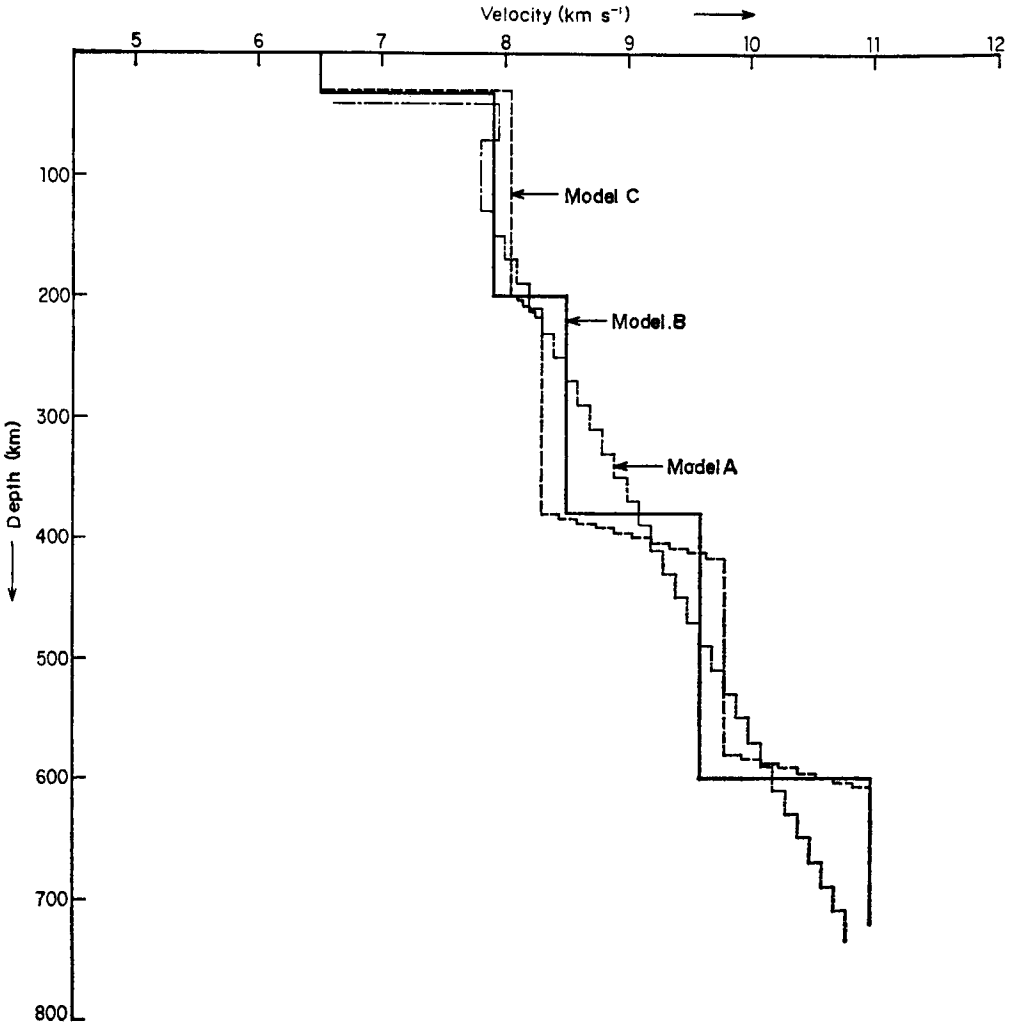


FIG. 6. Upper mantle models.

The calculations presented in this paper are much more sensitive to the $P$ velocity profile than to either the $S$ velocity profile or the density profile.

We begin our discussion of synthetic seismograms by computing the response, $u(t)$, for model A at a range of 20 degrees. We assume that the source is a pressure step. That is, we assume that the rise time of the pressure in the source cavity is short compared to periods of interest and that the decay time is long. We consider only those generalized rays that represent once reflected $P$ pulses. In generalized ray theory a reflected pulse has a precursor when the angle of critical reflection is exceeded. We call a wide angle reflection, one beyond the critical angle, a postcritical reflection. The beginning of the precursor is the head wave. The shape of the reflected pulse is altered to include not only its precritical shape but also its Hilbert transform. For example, if the precritical shape is a step, the postcritical shape will be composed of a step and a logarithmic singularity. The logarithmic singularity shows up as a 'spike' on the synthetic seismogram.

The synthetic seismogram for displacement as a function of time is denoted $SS(t)$. It is related to the response $u(t)$ and the pressure source function $S(t)$ by a convolution operation

$$\bar{S}\bar{S}(s) = s^2\,\bar{S}(s)\,\bar{u}(s) \tag{6}$$

where a typical expression for $\bar{u}$ is given by (5). The response $u(t)$ is, then, the time integrated displacement for a unit pressure step. This identification is forced on us by the degree of homogeneity in $s$ of the Cagniard–de Hoop integrand. No arbitrariness is involved in (6).

In (6) no account is taken of the fact that actual observations are made with a band limited instrument. We augment (6) by including the instrumentation response $I(t)$

$$\bar{S}\bar{S}(s) = s^2\,\bar{S}(s)\,\bar{u}(s)\,\bar{I}(s) \tag{7}$$

As a practical matter we have found it convenient to evaluate (7) as follows. First, $S(t)$ and $I(t)$ are convolved and the result differentiated to obtain a combined source-instrumentation function,

$$T(t) = \frac{d}{dt}\left(S(t)^* I(t)\right) \tag{8}$$

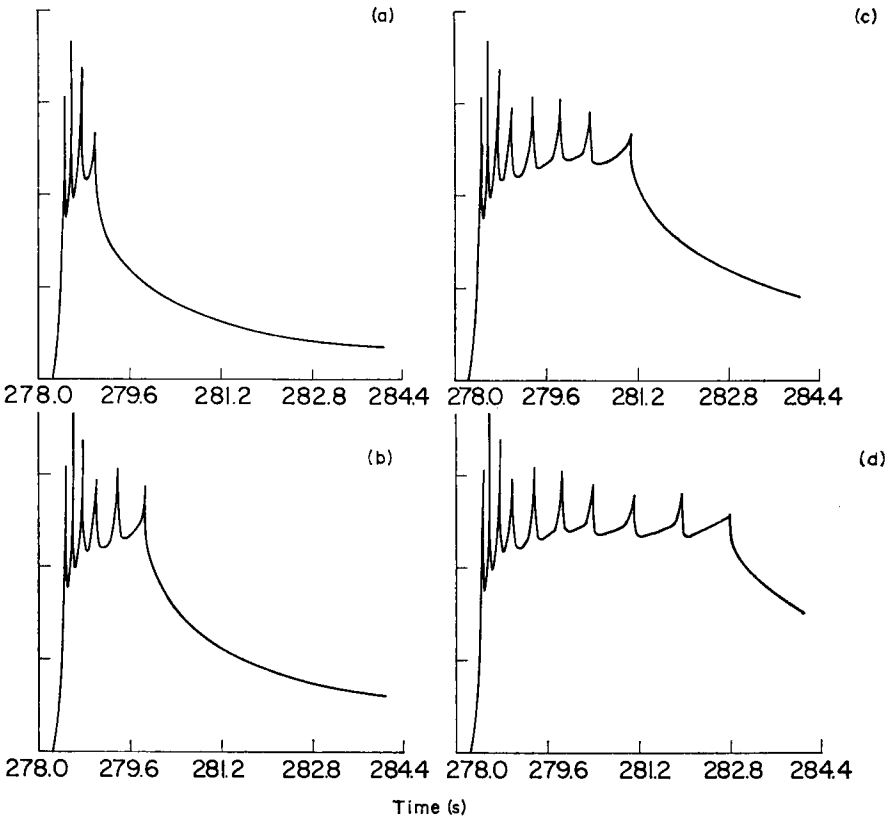


FIG. 7. Generalized ray summations, displaying the generation of a step function response.

Second, $u(t)$ is calculated by evaluating the relevant Cagniard–de Hoop expressions, convolved with $T(t)$ and the result differentiated to obtain the synthetic seismogram for displacement

$$SS(t) = \frac{d}{dt}(u(t)^* T(t)). \tag{9}$$

To see how the generalized ray response, $u(t)$, is built up, we refer to Fig. 7. In Fig. 7(a) there are four spikes. The first is the contribution from the ray reflected at a depth of 410 km. The next three represent the reflections from depths of 390, 370 and 350 km, respectively. All four rays are postcritical. In Fig. 7(b) we have included two more rays, from depths of 330 and 310 km, respectively. Fig. 7(c) and (d) show the effect of including more rays from successively shallower depths, and, therefore, rays that successively exceed their critical angles from the postcritical side. This accounts for the diminution in amplitude and the broadening of the spikes associated with the later arriving rays.

When a synthetic response such as that shown in Fig. 7(d) is filtered to reject high frequencies the result is a smooth, step-like function. Also, when the layering thick-

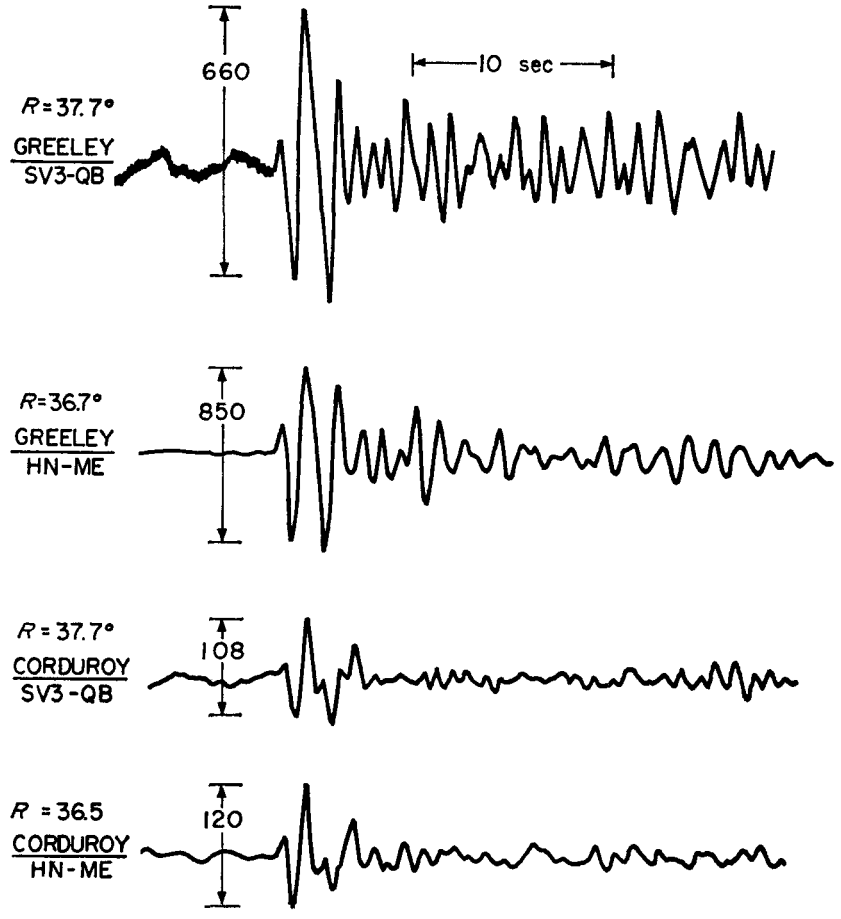


FIG. 8. Teleseismic recordings of NTS events GREELEY and CORDUROY.

ness is decreased, the amplitude of each spike decreases but the number per unit time increases, so that the frequency, below which the response looks like a step, increases. That is, a smooth mantle transmits a pulse without distortion, a well known and, consequently, unsurprising fact.

Model A, whose synthesized response at 20° is shown in Fig. 7, has a homogeneous crust. Such a model is too simple and we must, somehow, find a way to take into account crustal effects. There are two ways. We could consider a more complicated crustal model and, thereby, calculate a more complicated $u(t)$.

Alternatively, we can take advantage of the fact that teleseismic rays are nearly vertical near the source and the receiver. The crustal effect in this case is effectively that of an attenuating delay line. We could pretend that the crustal structure is simple but that the actual source function $S(t)$ is more complicated. If a receiving station could be found, under which the crustal structure is simple, and if $u(t)$ is nearly a step, as it is for model A, then the station's observed pulse shape is a good approximation to $T(t)$ in (8). The problem is to find a simple (transparent) crustal structure, or, nearly equally acceptable, a crustal structure common to two or more stations. The later problem can be solved by viewing recordings from one event at several stations.

An example is given in Fig. 8 for two stations and two events. In the upper two traces, for the GREELEY event, it is clear that the station in Quebec and the station in Maine have virtually identical pulse shapes for at least the first 5 s of the record. In the lower two traces, for the CORDUROY event, the pulse shape correspondence is equally obvious. We conclude that the two stations have a common crustal structure. The two events had different source depths and slightly different locations, which explains, at least partially, the difference in pulse shape.

If we adopt the approach just outlined, then we regard $T(t)$ as the combined representation of source function, instrumentation response, and crustal structure at both source and receiver. This simplifies our work because $u(t)$ is far easier to calculate for simple crusts than for complicated ones.

To illustrate the effect of a thin crustal layer above the source, we present Fig. 9. A layer of thickness 0·45 km, $P$ velocity 2·0 km s$^{-1}$, $S$ velocity 1·2 km s$^{-1}$ and density 2·4 g cm$^{-3}$ overlies a medium whose parameters are a $P$ velocity of 5·2 km s$^{-1}$, $S$ velocity 2·2 km s$^{-1}$ and density 2·6 g cm$^{-3}$. This medium contains an idealized pressure point source, denoted by the asterisk in the figure, at a depth of 0·30 km below the interface. We pick a point in the lower medium whose horizontal distance away from the source and vertical distance below the source correspond to the angle of incidence appropriate for emergence as a first arrival at a range of 3000 km. We refer to $u(t)$ calculated at this point as the 'downgoing response'.

The upper portion of Fig. 9 shows the downgoing response. In this calculation we have included all generalized rays beginning less than 4 s after the first arrival. The first arrival is, of course, the direct pulse. The reflection from the interface reduces the amplitude; this is followed by the surface $pP$ reflection. Successive arrivals correspond to multiple reflections within the layer. For the purposes of illustration we have chosen $I(t)$ from the work of Carpenter (1967, Fig. 4, $T/Q = 0{\cdot}75$). The source function, $S(t)$, is that of Toksöz & Clement (1967) for the BILBY event. The convolution of $u(t)$, $I(t)$, and $S(t)$ is shown in the lower half of Fig. 9. For a transparent path to the receiver this pulse shape should be the observed one. It is not unlike the pulse shapes in Fig. 8, and is a reasonable $T(t)$ to use for $NTS$ events.

We turn our attention now to a discussion of models $B$ and $C$, two simplified profiles containing abrupt changes in velocity in the upper mantle. Synthetic seismograms for model B are shown in Fig. 10. The function $T(t)$ used in the calculations is shown in the box. It is the observed response for the BILBY event at station HNME. For this station the calculated $u(t)$, for the first few seconds after onset, is virtually a step so that the observed pulse is a good approximation to $T(t)$. Station

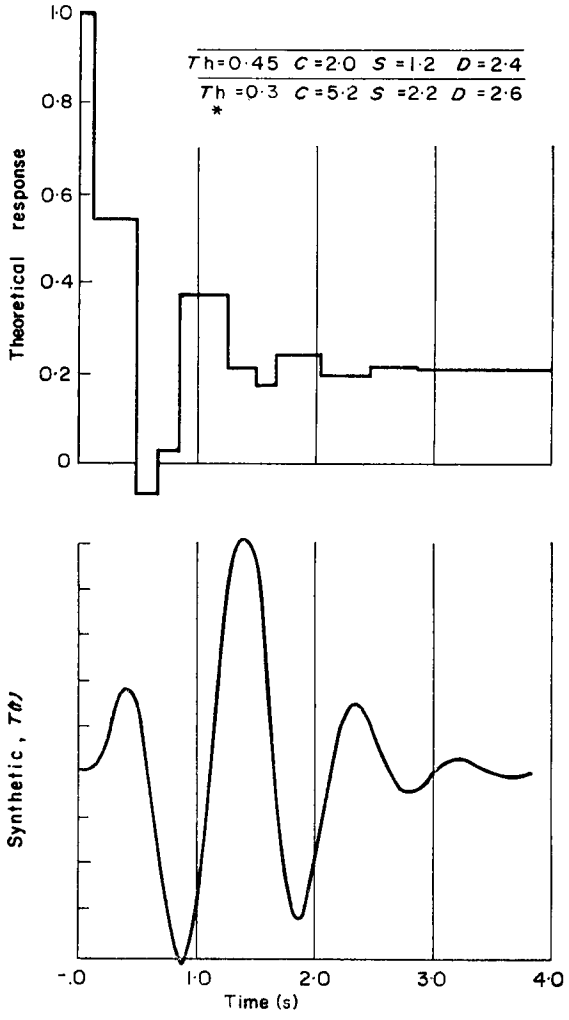


FIG. 9. Synthetic effective source function.

HNME is about 36·5° from the source, and its first arriving ray bottoms at a depth well below the discontinuities of model B and is, therefore, little affected by them.

Model B contains only four layers with discontinuities at depths of 200, 380 and 600 km. Reflections, whether precritical or postcritical, from these boundaries are denoted 2, 4 and 6, respectively, in Fig. 10. Only generalized *P* rays are included in the calculations. First multiple reflections are included but primary reflections dominate the motion. The critical angles for the 2, 4 and 6 reflections are 11°, 13°, and 17°, respectively. The seismograms become relatively complex at the critical angles even though the motion is represented, for the most part, by only two or three generalized rays. Beyond the critical angle for a particular generalized ray, one can see the onset of the precursive head wave, or refraction, that arrives before the postcritical reflection. It is important to emphasize, once again, that the postcritical reflection and its precursive head wave represent the response of a single generalized ray.

The main difference between models B and C is that the major discontinuities in

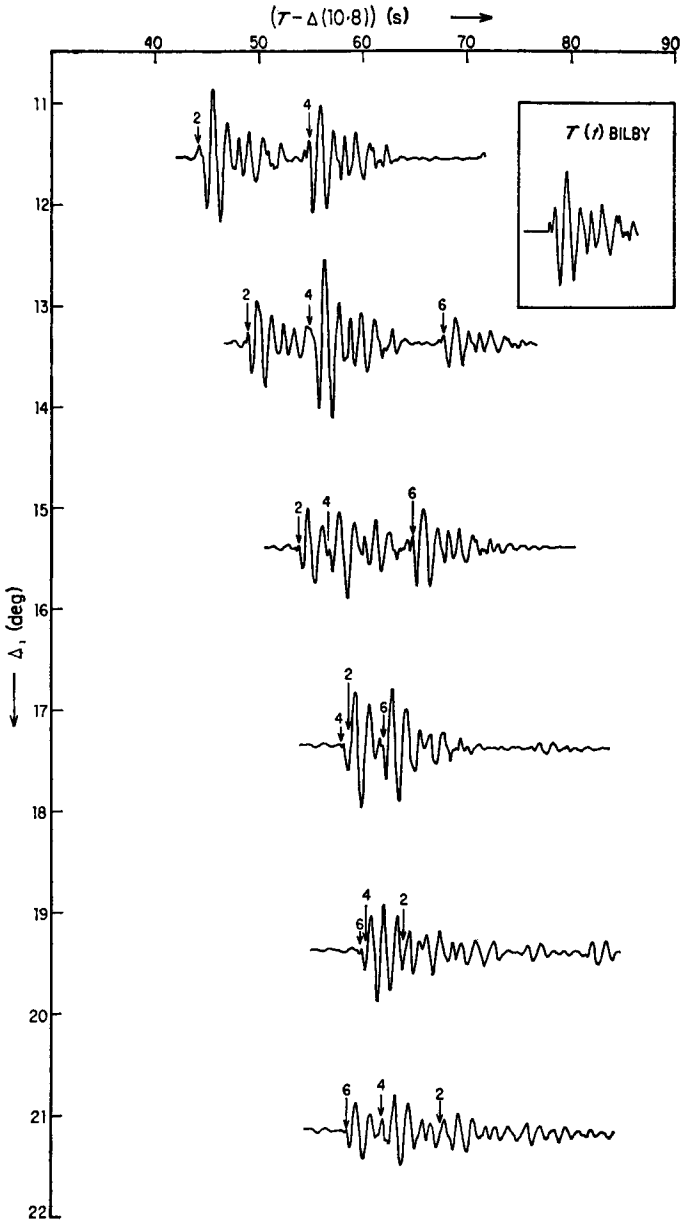


FIG. 10. Synthetic seismograms based on model B.

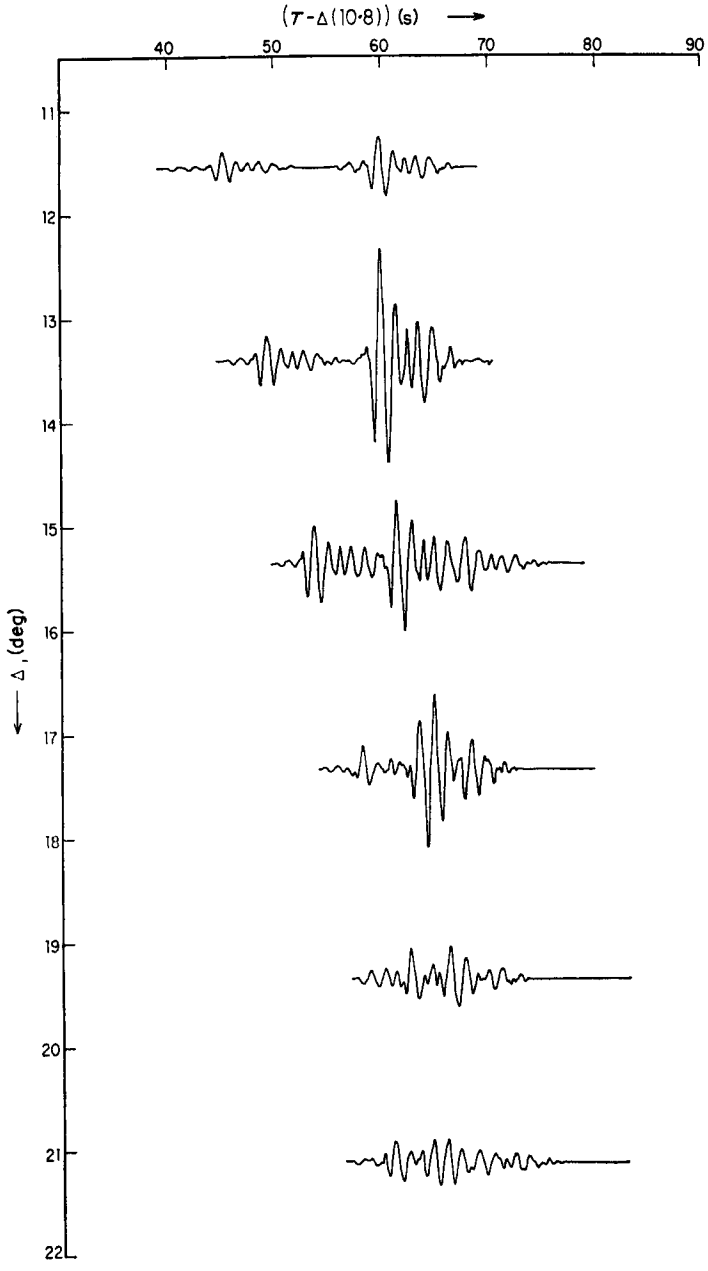


FIG. 11. Synthetic seismograms based on model C.

*B* are replaced by gradients, albeit the gradients are themselves modelled as a series of steps. Synthetic seismograms for model C are shown in Fig. 11. The function T (*t*) is the same one used for model B in Fig. 10.

Replacing a discontinuity by a gradient enhances the amplitude near the critical angle and reduces it elsewhere. This effect is particularly noticeable for the 4-reflection from 11° to 15°. The 6-reflection is more difficult to identify in Fig. 11 than in Fig. 10 because it interferes with the 4-reflection where the latter is strong. Finally, model C has a larger average velocity in the upper mantle, and consequently, its first arrivals occur slightly earlier.

In this preliminary presentation of synthetic seismograms for models of the upper mantle, we observe that the rôle of head waves, or refractions, along deep interfaces is of minor importance. As we have mentioned in the previous section, we have neglected entirely the contribution from a theoretically less significant kind of ray—the chord ray. Neglecting the chord ray appears to be justified.

## Comparison of synthetics with observations

The record section from model C shown in Fig. 11 shows many similarities with the NE profile shown in Fig. 4 at the shorter ranges. The large second arrival occurring at 60 s is apparent in both the synthetics and observations. This feature appears at 11° and is strong at 12° as indicated in Fig. 23 of Julian & Anderson (1968). The observed first arrival is generally small throughout these ranges, becoming very small for ranges greater than 15°. The corresponding synthetics tend to grow with range, which means the 2-transition, the transition zone at about 200 km depth, is slightly deeper than in the model. There appears to be little correspondence between the synthetics and observations at ranges greater than 17°. The most noticeable difference is the large first arrival occuring in the observations between 19° and 21°. This is absent in the synthetics. This feature of the observations cannot be explained by having a smooth mantle between depths of 450 and 600 km. The 6-transition is not very apparent in the NE profile. This may be caused by the domination of the 4-reflection.

The situation in the SE profile is quite different. In this profile there is little evidence of the arrival from the 4-transition before 14°. This could be caused by a strong first arrival coming from shallow depths or perhaps a smaller 4-transition. If the latter is true it would explain why the arrival from the 6-transition is more apparent than in the NE profile.

Comparing the synthetics from model B with the SE profile one sees many similarities. In fact it appears that if the bottom interface in model B were lowered such that the crossover between 4 and 6 occurred at 21° the correspondence would be quite good. A more detailed study of the structure of the upper mantle, using more data, including earthquakes, and more refined models is the subject of a paper by Helmberger & Wiggins (1971).

## Acknowledgment

This research was supported by the Advanced Research Projects Agency of the Department of Defense and was monitored by the Air Force Office of Scientific Research under Contract No. F44620-69-C-0118 and AF49(638)-1763.

Freeman Gilbert:

*Institute of Geophysics and Planetary Physics*
*and Scripps Institution of Oceanography,*
*University of California,*
*San Diego, La Jolla,*
*California.*

Donald V. Helmberger:

*Department of Earth and Planetary Science,*
*Massachusetts Institute of Technology,*
*Cambridge,*
*Massachusetts.*



## References

Cagniard, L., 1939. *Reflexion et refraction des ondes seismiques progressives*, Gauther-Villars, Paris.

Cagniard, L., 1962. *Reflexion and refraction of progressive seismic waves*, translated by E. A. Flinn and C. H. Dix, McGraw-Hill, New York.

Carpenter, E. W., 1967. Teleseismic signals calculated for underground, underwater, and atmospheric explosions, *Geophysics* **32,** 17–32.

Hoop, A. T. de, 1960. A modification of Cagniard's Method for solving seismic pulse problems, *Appl. Sci. Res.*, **B8**, 349–356.

Dougall, J., 1900. The determination of Green's Function by means of cylindrical or spherical harmonics, *Proc. Edin. math. Soc.*, **18,** 33–83.

Dowling, J. & Nutti, O., 1964. Travel-time curves for a low-velocity channel in the upper mantle, *Bull. seism. Soc. Am.*, **54,** 1981–1996.

Erdelyi, A., Magnus, W., Oberhettinger, F. & Tricomi, F. G., 1953. Higher transcendental functions, Vol. 2, *Bateman Manuscript Project,* McGraw-Hill, New York.

Friedlander, F. G., 1954. Diffraction of pulses by a circular cylinder, *Comm. pure appl. math.*, **7,** 705–732.

Helmberger, D. & Wiggins, R. A., 1971. Upper mantle structure of midwestern United States, *J. geophys. Res.*, **76,** 3229–3245.

Johnson, L. R., 1967, Array measurements of *P*-velocities in the Upper Mantle, *J. geophys. Res.*, **72,** 6309–6325.

Julian, B. R. & Anderson, D. L., 1968. Travel times, apparent velocities and amplitudes of body waves, *Bull. seism. Soc. Am.*, **58,** 339–366.

Keller, J. B., 1957. Diffraction by an aperture, *J. appl. Phys.*, **28,** 426–444.

Keller, J. B., 1958. How dark is the shadow of a round-ended screen? *N.Y.U. Technical Report* EM-119.

Knopoff, L. & Gilbert, F., 1959. First motion methods in theoretical seismology, *J. acoust. Soc. Am.*, **31,** 1131–1139.

Lamb, H., 1904. On the propagation of tremors over the surface of an elastic solid, *Phil. Trans. R. Soc. Lond.*, **A203,** 1–42.

Nussenzveig, H.M., 1965. High-frequency scattering by an impenetrable sphere, *Ann. Phys.*, **34,** 23–95.

Pekeris, C. L., 1948. Theory of propagation of explosive sound in shallow water, *G.S.A. Memoir*, **27,** 46–51.

Scholte, J. G. J., 1956. On seismic waves in a spherical earth, *Kononkl. Ned. Meteorol. Inst. Publ.*, **65,** 9–55.

Spencer, T., 1960. The method of generalized reflection and transmission coefficients, *Geophysics*, **25**, 625–641.

Szegö, G., 1934. Über einige asymptotische Entwicklungen der Legendreschen Functionen, *Proc. Lond. Math. Soc.*, **36**, 427–450.

Titchmarsh, E. C., 1952. *The theory of Functions.* 2nd ed., Oxford University Press.

Toksöz, M. N. & Clement, K., 1967. Radiation of seismic waves from the Bilby explosion, *Report prepared for Air Force Technical Applications Center*, Washington, D.C.

Weyl, H., 1919. Ausbreitung der elektromagnetischer Wellen, *Ann. Phys.*, **60**, 481–500.

## Appendix A

In this paper we have shown how to apply generalized ray theory to a sphere composed of concentric, homogeneous, spherical shells. We make the traditional approximations as if we were preparing to use the saddle-point method to obtain the geometrical ray approximation. A simple change of variable, based on Lamb's (1904) observation that the eikonal is linear in the frequency, allows us to apply the method of Cagniard (1939, 1962) and de Hoop (1960), so that the transient solution is found by inspection. The result is an approximation in the time domain valid for pulses of short duration, but more useful than the first-motion approximation (Knopoff & Gilbert 1959). As the curvature of the spherical layers approaches zero, the approximate transient solution for spherical layers approaches the *exact* transient solution for plane layers. The method is readily illustrated by an example, the reflection of an *SH* pulse by a sphere (Fig. 12). First we consider the sphere to be fixed and rigid.

In spherical polar coordinates $(r, \theta, \phi)$ the equation to be solved is

$$\mu\nabla^2 u(r,\theta,t) - \rho\frac{\partial^2 u}{\partial t^2}(r,\theta,t) = -\frac{f(t)\delta(r-r_0)\delta(\theta-0^+)}{2\pi r^2 \sin\theta}. \tag{A.1}$$

For $t < 0$ we assume $f(t) \equiv 0$, $u \equiv 0$, $\partial u/\partial t \equiv 0$. The boundary condition is $u(a, \theta, t) = 0$. We attack the initial value-boundary value problem in a traditional way; we separate variables by a series of transformations. Let

$$\bar{u}(r,\theta;s) = \int_0^\infty u(r,\theta;t)\exp(-st)\,dt \tag{A.2}$$

and confine $s$ to positive real values. Then the Laplace transform of (A.1) is

$$\nabla^2\bar{u} - \frac{s^2\bar{u}}{\beta^2} = -\frac{\bar{f}(s)\delta(r-r_0)\delta(\theta-0^+)}{2\pi\mu r^2\sin\theta} \tag{A.3}$$

where $k = s/\beta$, $\beta$ being the shear velocity.

Continuing, we let

$$U(r;l,s) = \int_0^\pi \bar{u}(r,\theta;s)\,P_l(\cos\theta)\sin\theta\,d\theta. \tag{A.4}$$

Then, the Legendre transform of (A.3) is

$$\frac{1}{r^2}\frac{d}{dr}\left(r^2\frac{d}{dr}U\right) - \left(k^2 + \frac{l(l+1)}{r^2}\right)U = -\frac{\bar{f}(s)\delta(r-r_0)}{2\pi\mu r^2}. \tag{A.5}$$

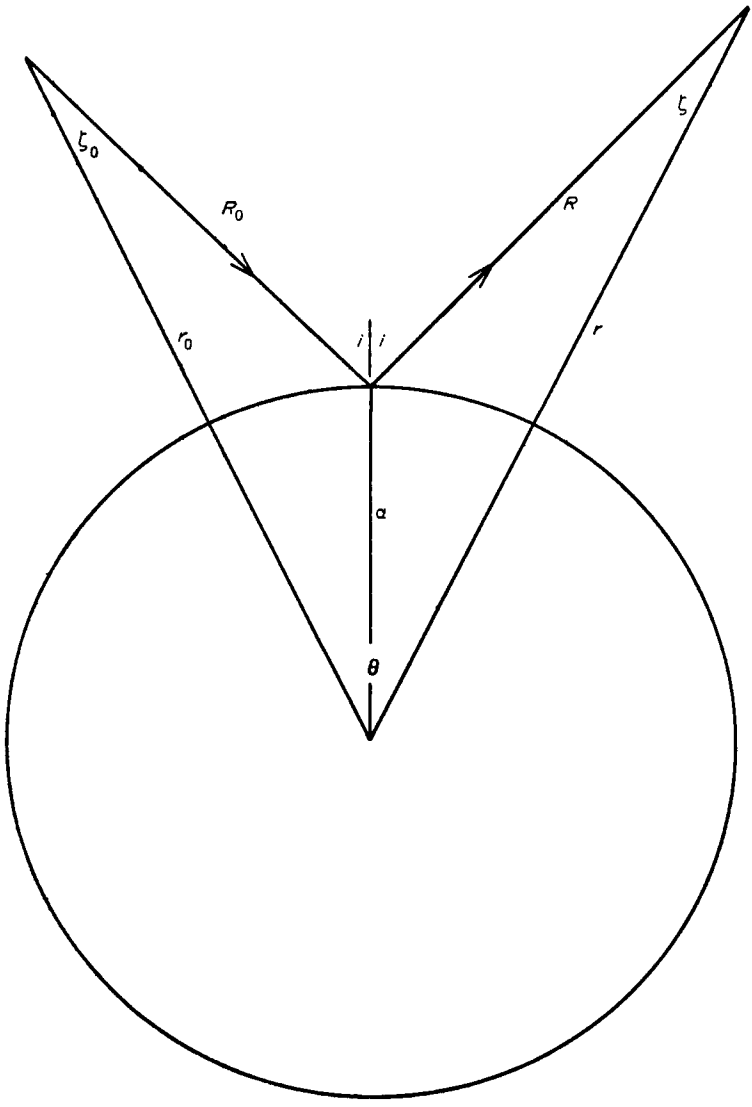


FIG. 12. Ray path and angles used in the geometrical interpretation of saddlepoint in the *SH* reflection problem.

The solution to (A.5) that satisfies the boundary condition and the radiation condition is

$$U(r;l,s)=\frac{k\bar{f}(s)}{\pi^2\mu}\left[\imath_l(kr_<)\,\kappa_l(kr_>)-\frac{\imath_l(ka)\,\kappa_l(kr_0)\,\kappa_l(kr)}{\kappa_l(ka)}\right] \tag{A.6}$$

where $\imath$ and $\kappa$ are modified spherical Bessel functions of the first and second kind, respectively.

Once $U$ is known we have

$$\bar{u}(r;\theta,s)=\sum_{l=0}^{\infty}(l+1/2)\,U(r;l,s)\,P_l(\cos\theta). \tag{A.7}$$

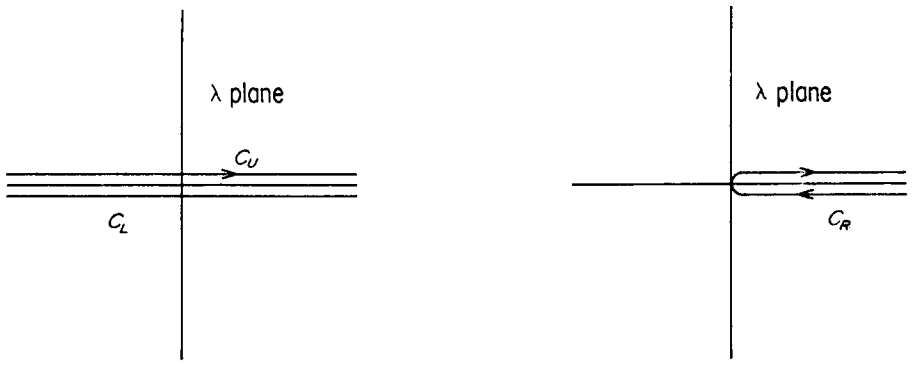


FIG. 13. Integration contours for the Watson transformation.

For short pulses ($ka \gg 1$) (A.7) is virtually useless. The series begins to converge after $L$ terms where $L \sim (ka)+c(ka)^{\frac{1}{3}}$ and $c$ is a positive constant of order unity. The remedy is classical; we rewrite (7) by using the Watson transformation. (A simple exposition of this transformation is presented by Titchmarsh (1952, p. 114). One of its first applications to mathematical physics was made by Dougall (1900)). The identity,

$$\sum_{l=0}^{\infty} \mathscr{F}(l+\tfrac{1}{2}) = \frac{1}{2} \int_{C_R} \mathscr{F}(\lambda) \sec \lambda\pi \exp(-i\lambda\pi)\, d\lambda \tag{A.8}$$

where $C_R$ is shown in Fig. 13, is used to convert series, such as (7) into contour integrals. Obviously, there is some degree of arbitrariness in the definition of $\mathscr{F}(\lambda)$ in (A.8). All that is required is that $\mathscr{F}(\lambda)$ be an analytic function of $\lambda$ in a domain including $C_R$ and the right real $-\lambda$ axis. We apply (A.8) to (7) and use the relation

$$P_l(\cos\theta) = \exp(il\pi)\, P_l(\cos(\pi-\theta))$$

to obtain

$$\bar{u}(r,\theta;s) = \frac{1}{2i} \int_{C_R} \lambda \sec \lambda\pi\, P_{\lambda-\frac{1}{2}}(\cos(\pi-\theta))\, U(r;\lambda-\tfrac{1}{2},s)\, d\lambda. \tag{A.9}$$

Expressing the spherical Bessel functions in (A.6) in terms of cylindrical Bessel functions we write (A.9) as

$$\bar{u} = \frac{\bar{f}(s)}{4\pi i\mu(rr_0)^{\frac{1}{2}}} \int_{C_R} \lambda \sec \lambda\pi\, P_{\lambda-\frac{1}{2}}(\cos(\pi-\theta))\, \mathscr{K}(\lambda)\, d\lambda \tag{A.10}$$

where

$$\mathscr{K}(\lambda) = \left[ I_\lambda(kr_<)\, K_\lambda(kr_>) - \frac{I_\lambda(ka)\, K_\lambda(kr_0)\, K_\lambda(kr)}{K_\lambda(ka)} \right]. \tag{A.11}$$

For large $k$ (short pulses) the dominant contribution to the integral in (A.10) comes from values of $\lambda \gg 1$, $\lambda \approx ka$. Following the traditional approach we replace the Bessel functions in (11) by approximations valid for large $\lambda$. To obtain the

classical ray-theoretical results we use the approximations (Erdelyi *et al.* 1953)

$$\left.\begin{aligned} I_\lambda(x) &= \frac{\exp(\xi)}{(2\pi)^{\frac{1}{2}}(x^2+\lambda^2)^{\frac{1}{4}}}[1+0(\lambda^{-1})] \\ K_\lambda(x) &= \frac{\exp(-\xi)}{(2/\pi)^{\frac{1}{2}}(x^2+\lambda^2)^{\frac{1}{4}}}[1+0(\lambda^{-1})] \\ \xi &= (x^2+\lambda^2)^{\frac{1}{2}}-\lambda \sinh^{-1}(\lambda/x) \end{aligned}\right\} \tag{A.12}$$

and cut the $\lambda$ plane so that $\mathscr{R}e(x^2+\lambda^2)^{\frac{1}{2}} \geqslant 0$. Using (A.12) in (A.11) we see that $\mathscr{K}(\lambda)$ becomes an even function of $\lambda$. That, and the relation $P_\nu(\cos\theta) = P_{-\nu-1}(\cos\theta)$, show that the integrand in (A.10) is an odd function of $\lambda$. Thus, $C_R$ can be replaced by either $C_U$ or $C_L$. Parenthetically, we point out that $\lambda \sec\lambda\pi$ in (A.10), an odd function, can be replaced by $\lambda \sec\lambda\pi/[1-2\pi^{-2}\cos^2\pi\lambda\psi'(\lambda+\frac{1}{2})]$, an even function, so that (A.10) still leads to (A.7). In the preceding expression $\psi$ is the digamma function. Here is but one example of the arbitrariness mentioned following (A.8).

Henceforth, we confine our attention to the second term in (A.11) representing the reflected pulse in the geometrical ray region. Using (A.12) in (A.10) and (A.11) we have, for the Laplace transform of the reflected pulse,

$$\left.\begin{aligned} \bar{u} &= -\frac{\bar{f}(s)}{8\pi i\mu(rr_0)^{\frac{1}{2}}}\int_{i\varepsilon-\infty}^{i\varepsilon+\infty}\frac{\lambda \sec\lambda\pi P_{\lambda-\frac{1}{2}}(\cos(\pi-\theta))\exp(-\Phi)}{(k^2r_0{}^2+\lambda^2)^{\frac{1}{4}}(k^2r^2+\lambda^2)^{\frac{1}{4}}}\,d\lambda \\ \Phi &= (k^2r_0{}^2+\lambda^2)^{\frac{1}{2}}+(k^2r^2+\lambda^2)^{\frac{1}{2}}-2(k^2a^2+\lambda^2)^{\frac{1}{2}} \\ &\quad -\lambda \sinh^{-1}\lambda/kr_0-\lambda \sinh^{-1}\lambda/kr+2\lambda \sinh^{-1}\lambda/ka \\ &= \int_{ka}^{kr_0} x^{-1}(x^2+\lambda^2)^{\frac{1}{2}}\,dx+\int_{ka}^{kr} x^{-1}(x^2+\lambda^2)^{\frac{1}{2}}\,dx. \end{aligned}\right\} \tag{A.13}$$

Next we make an unnecessary but suggestive change of notation to emphasize more strongly the application of the Cagniard–de Hoop method. Let $\lambda = iv$ in (A.13). Applying Schwarz's reflection principle gives

$$\left.\begin{aligned} \bar{u} &= -\frac{\bar{f}(s)}{4\pi\mu(rr_0)^{\frac{1}{2}}}\,\mathscr{L}m\int_{\varepsilon}^{\varepsilon+i\infty}\frac{v \sec hv\pi P_{iv-\frac{1}{2}}(\cos(\pi-\theta))\exp(-\Psi)}{(k^2r_0{}^2-v^2)^{\frac{1}{4}}(k^2r^2-v^2)^{\frac{1}{4}}}\,dv \\ \Psi &= \Phi(iv) = \int_{ka}^{kr_0}+\int_{ka}^{kr} x^{-1}(x^2-v^2)^{\frac{1}{2}}\,dx \end{aligned}\right\} \tag{A.14}$$

and we require $\mathscr{R}e(x^2-v^2)^{\frac{1}{2}} \geqslant 0$.

It has been shown by Friedlander (1954) that the $v$-integral in (A.14) can be evaluated by the saddle point method to give $\bar{u}$ for the reflected pulse. The saddle point occurs on the real $v$ axis, $v \gg 1$, $v \leqslant ka$, where the approximations

$$\left.\begin{aligned} \sec hv\pi &= 2\exp(-v\pi)[1+0(\exp(-2v\pi))] \\ P_{iv-\frac{1}{2}}(\cos(\pi-\theta)) &= \frac{\exp[v(\pi-\theta)]}{(2\pi v\sin\theta)^{\frac{1}{2}}}[1+0(v^{-1})] \end{aligned}\right\} \tag{A.15}$$

are valid. Substituting (15) into (14) gives

$$\bar{u} = \frac{\bar{f}(s)}{2\pi\mu(2\pi r r_0 \sin\theta)^{\frac{1}{2}}} \mathscr{L}m \int_{\varepsilon}^{\varepsilon+i\infty} \frac{v^{\frac{1}{2}} \exp(-v\theta - \Psi)}{(k^2 r_0{}^2 - v^2)^{\frac{1}{2}} (k^2 r^2 - v^2)^{\frac{1}{2}}} dv. \tag{A.16}$$

A better approximation than (A.15) is given by Szegö (1934)

$$P_{\lambda-\frac{1}{2}}(\cos\theta) = \left(\frac{\theta}{\sin\theta}\right)^{\frac{1}{2}} [J_0(\lambda\theta) + 0(\lambda^{-1})]. \tag{A.16a}$$

The use of (A.16a) in the following development leads to the Bessel function $K_0(s\gamma\theta)$ in (5). The cruder approximation (A.15) is used here for clarity of exposition.

The next step in the classical programme is the evaluation of (A.16) by the method of steepest descent, or, more usually, by the saddle-point method. At this point we leave the classical programme and make the change of variable $v = s\gamma$, and recall that $s$ is real and positive,

$$\left.\begin{aligned} \bar{u} &= \frac{-\bar{f}(s)\, s^{\frac{1}{2}}}{2\pi\mu(2\pi r r_0 \sin\theta)^{\frac{1}{2}}} \mathscr{L}m \int_{C}^{C+i\infty} \frac{\gamma^{\frac{1}{2}} \exp[-s(\gamma\theta+\psi)]}{(r_0{}^2/\beta^2 - \gamma^2)^{\frac{1}{2}} (r^2/\beta^2 - \gamma^2)^{\frac{1}{2}}} d\gamma \\ \psi &= \int_a^{r_0} + \int_a^{r} y^{-1}(y^2/\beta^2 - \gamma)^{\frac{1}{2}}\, dy \\ &= (r_0{}^2/\beta^2 - \gamma^2)^{\frac{1}{2}} + (r^2/\beta^2 - \gamma^2)^{\frac{1}{2}} - 2(a^2/\beta^2 - \gamma^2)^{\frac{1}{2}} \\ &\quad + \gamma(\sin^{-1}\gamma\mu/r_0 + \sin^{-1}\gamma\beta/r - 2\sin^{-1}\gamma\beta/a). \end{aligned}\right\} \tag{A.17}$$

In (17) let

$$\left.\begin{aligned} \mathscr{C}\bar{f}(s)\, s^{\frac{1}{2}} &= \int_0^{\infty} w(t) \exp(-st)\, st \\ \mathscr{C} &= 1/[2\pi\mu(2\pi r r_0 \sin\theta)^{\frac{1}{2}}] \\ \mathscr{G}(\gamma) &= \gamma^{\frac{1}{2}}(r_0{}^2/\beta^2 - \gamma^2)^{-\frac{1}{2}} (r^2/\beta^2 - \gamma^2)^{-\frac{1}{2}} \end{aligned}\right\} \tag{A.18}$$

$$\left.\begin{aligned} \bar{v} &= -\mathscr{L}m \int_C^{C+i\infty} \mathscr{G}(\gamma) \exp[-s(\gamma\theta+\psi)]\, d\gamma \\ \bar{v} &= \int_0^{\infty} v(r,\theta,t) \exp(-st)\, dt. \end{aligned}\right\} \tag{A.19}$$

Then

$$u(t) = w(t)^* v(t)$$

and our task becomes to solve (19) for $u(t)$. We must find a curve in the first quadrant of the $\gamma$-plane along which $(\gamma\theta+\psi)$ is real so that the two exponents in (19) can be equated. Consider $|\gamma| \gg 1$ and $t \gg 1$. Then from (17), for large $|\gamma|$

$$\left.\begin{aligned} \psi &\simeq -i\gamma \log r r_0/a^2 \\ \gamma\theta+\psi &\simeq \gamma\theta - i\gamma \log r r_0/a^2. \end{aligned}\right\} \tag{A.20}$$

Therefore, for large $\gamma$ and $t$, the curve sought is

$$\gamma = t/(\theta - i \log rr_0/a^2) \tag{A.21}$$

a straight line in the first quadrant of the $\gamma$-plane. The curve $\gamma\theta+\psi = t$ is asymptotic to the line (21) for large $t$. Although we make no use of it in this paper, we remark that the asymptote (21) exists regardless of whether the observation point $(r, \theta)$ is in the region of the geometrical ray (the lit or illuminated region), or in the shadow zone. This suggests the interesting possibility that diffraction phenomena can be examined by generalized ray theory.

Another important property of the curve $\gamma\theta+\psi = t$ is the point $\gamma_0$ where it touches the real $-\gamma$ axis. In the classical programme the saddle point lies on the real axis where the exponent is real ($\gamma \leqslant a/\beta$). Along the path of steepest descent the imaginary part of the exponent has a constant value equal to its value at the saddle point; namely, zero. Therefore, the curve $\gamma\theta+\psi = t$ is the path of steepest descent and it touches the real axis at $\gamma_0$ where

$$\theta + \frac{d\psi}{d\gamma}\bigg|_{\gamma_0} = 0. \tag{A.22}$$

From (17) we find

$$\frac{d\psi}{d\gamma} = \sin^{-1}\gamma\beta/r_0 + \sin^{-1}\gamma\beta/r - 2\sin^{-1}\gamma\beta/a. \tag{A.23}$$

The usual geometrical interpretation of the saddle point is made by regarding $\gamma_0$ as a ray parameter (see Fig. 12)

$$\gamma_0 = \beta^{-1} r_0 \sin\zeta_0 = \beta^{-1} r \sin\zeta = \beta^{-1} a \sin i. \tag{A.24}$$

Summing the angles of the two triangles in Fig. 12 shows that (24) satisfies (22). Let $t_0 = \gamma_0\theta+\psi(\gamma_0)$. For $t = t_0+\delta t$, $\delta t \ll t_0$, a short calculation shows that the solution to $\gamma\theta+\psi = t$ is

$$\gamma = \gamma_0 + i(\delta t)^{\frac{1}{2}} \left[\frac{2a\, rr_0 \cos i \cos\zeta \cos\zeta_0}{\beta(R_0\, r\cos\zeta + Rr_0 \cos\zeta_0)}\right]^{\frac{1}{2}} + 0(\delta t). \tag{A.25}$$

Thus, the Cagniard path, as it is customarily called, is perpendicular to the real axis at the saddle point $\gamma_0$ and approaches the line (21) asymptotically for large $t$ (Fig. 14). It is now clear how to solve (19) for $v(r, \theta, t)$. Since $\mathscr{G}(\gamma)$ is real for $0 \leqslant \gamma \leqslant a/\beta$ we can set $C = \gamma_0$ without loss of generality. From (20) we see that $\mathscr{R}e(\gamma\theta+\psi) > 0$ for large $\gamma$ in the first quadrant. Invoking Jordan's lemma, we replace the $\gamma$-integration variable from $\gamma$ to $t$

$$\bar{v} = -\mathscr{I}m \int_{t_0}^{\infty} \mathscr{G}(\gamma(t)) \exp(-st)(d\gamma/dt)\, dt. \tag{A.26}$$

Comparing (26) to the second part of (19) we have

$$-\mathscr{I}m \int_{t_0}^{\infty} \mathscr{G}(\gamma(t)) \exp(-st)(d\gamma/dt)\, dt = \int_0^{\infty} v(t) \exp(-st)\, dt \tag{A.27}$$

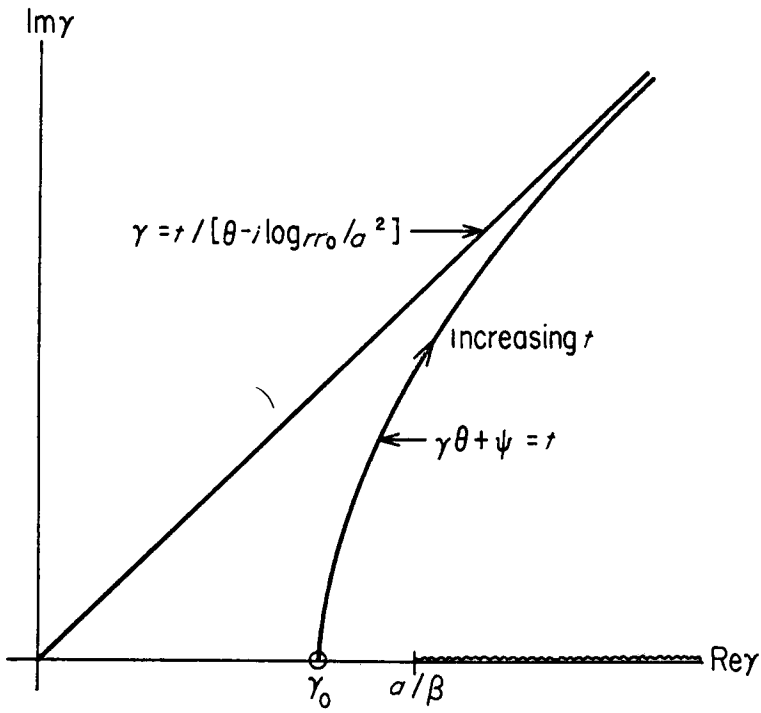


FIG. 14. Typical Cagniard–deHoop contour and its asymptote.

for all real positive $s$. Lerch's theorem assures us that

$$v(t) = \mathscr{L}m\left[-\mathscr{G}(\gamma(t))\frac{d\gamma}{dt}\right]H(t-t_0) \tag{A.28}$$

where $\gamma(t)$ is the solution in the first quadrant to $\gamma\theta+\psi = t$. According to (25) $v(t)$ has a first motion proportional to $(t-t_0)^{-\frac{1}{2}}$. Convolution with $w(t)$ in (18) shows that $u(r, \theta, t)$ has a first motion proportional to $f(t)$.

As a second example we consider the case where the material $r > a$ is denoted by $(\mu_1, \rho_1)$ and the material $r < a$ by $(\mu_2, \rho_2)$. The result is that (28) is replaced by

$$v(t) = \mathscr{L}m\left[\mathscr{R}(\gamma/a)\,\mathscr{G}(\gamma)\frac{d\gamma}{dt}\right]H(t-t_0) \tag{A.29}$$

where

$$\mathscr{R}(p) = \frac{\mu_1\eta_1(p)-\mu_2\eta_2(p)}{\mu_1\eta_1(p)+\mu_2\eta_2(p)} \tag{A.30}$$

and $\eta = (1/\beta^2-p^2)^{\frac{1}{2}}$, $\mathscr{R}e(\eta) \geqslant 0$. If we think of $p$ as a ray parameter $(\sin i/\beta)$ in a plane stratified medium we recognize $\mathscr{R}(p)$ as the plane-wave reflection coefficient.

The extension of this theory to multi-layered media parallels that for plane layers. The reflection and transmission coefficients for a plane interface can be used; a slowness factor such as $(\beta^{-2}-p^2)^{\frac{1}{2}}$, where $p$ is the ray parameter for plane layers, is replaced by $(\beta^{-2}-\gamma^2/r^2)^{\frac{1}{2}}$, where $\gamma$ is the ray parameter for spherical layers and $r$

is the radius of the interface to which the reflection or transmission coefficient is assigned. The exponent $\psi$ in a plane stratified medium can be written

$$\psi_{\text{plane}} = \int^{z} (\beta^{-2} - p^2)^{\frac{1}{2}} dz$$

while for a spherically stratified medium

$$\psi_{\text{sphere}} = \int^{r} (\beta^{-2} - \gamma^2/r^2)^{\frac{1}{2}} dr$$

and these two expressions are directly related to (1) and (3) in the main text.

## Appendix B

The Laplace inversion of integrals such as (B.4) or (B.5) in the main text is clarified by the use of operational methods. Consider the expression for the Laplace transform of the displacement associated with a typical generalized ray

$$\bar{u}(s) = \frac{1}{\pi i} \int_{F}^{U(p)} K_n(spR) \exp(-s\psi)\, dp. \tag{B.1}$$

In (B.1) $U(p)$ is an algebraic function of $p$ and $\eta$ where $\eta = (v^{-2} - p^2)^{\frac{1}{2}}$. Let $c = \min(v^{-1})$. Then $U(p)$ is real when $p$ is real, $-c \leqslant p \leqslant c$. A typical expression for $\psi$ is given in the equation following (B.4) in the main text. Because of the symmetry of the integrand we can replace (B.1) by

$$\bar{u}(s) = \frac{2}{\pi} \mathscr{I}m \int_{0}^{i\infty} U(p)\, K_n(spR) \exp(-s\psi)\, dp. \tag{B.2}$$

In (2) $K_n$ is proportional to $\exp(-spR)$ for large $|p|$, and $\mathrm{Re}\,\psi \leqslant 0$ for large $|p|$. Consequently $\mathrm{Re}(pR+\psi) > 0$ in the first quadrant of the $p$-plane and the integrand vanishes exponentially as $|p| \to \infty$. We use Jordan's lemma to deform the contour in (2) onto the contour $\mathscr{I}m(pR+\psi) = 0$ in the first quadrant. We recognize the latter contour as the Cagniard path, which we denote by $\tau(p)$. The value $\tau(0)$ is the vertical reflection time, the earliest possible arrival time for the generalized ray represented by (B.2). Consequently $u(t) = 0$ for $t < \tau(0)$. We can, in principle, solve the equation

$$pR + \psi = \tau;\ \tau \geqslant \tau(0) \tag{B.3}$$

for $p$ as a function of $\tau$ along the Cagniard path.

Thus, we change integration variables in (B.2) from complex $p$ to real $\tau$

$$\bar{u}(s) = \frac{2}{\pi} \mathscr{I}m \int_{\tau(0)}^{\infty} U(p)\, K_n(spR) \exp(-s\psi) \frac{dp}{d\tau} d\tau \tag{B.4}$$

Equation (4) is easily inverted by operational methods now that the Cagniard path has been chosen. The operational image of $K_n(spR)\exp(-s\psi)$ is

$$K_n(spR)\exp(-s\psi) \Leftrightarrow \frac{H(t-\tau)\cos h\{n \cos h^{-1}[(t-\psi)/pR]\}}{[(t-\psi)^2 - p^2 R^2]^{\frac{1}{2}}}. \tag{B.5}$$

Now we can use (5) to write the operational image of (4)

$$u(t) = \frac{2}{\pi} \mathscr{I}m \int_{\tau(0)}^{t} U(p) \frac{dp}{d\tau} \frac{\cos h\{n \cos h^{-1}[(t-\psi)/pR]\}}{[(t-\psi)^2 - p^2 R^2]^{\frac{1}{2}}} d\tau. \tag{B.6}$$

It is sometimes helpful to break the integral in (B.6) into two parts. Let $p_0$ be the saddlepoint $(d/dp)(pR+\psi)|_{p_0} = 0$ and let $t_0 = \tau(p_0)$. Let $p_1$ be the branch point of $U(p)$ nearest the origin, $p_1 \geqslant c = \min(v^{-1})$. If $p_1 \geqslant p_0$ we replace $\tau(0)$ in (B.6) by $t_0$. There is no head wave. If $p_1 < p_0$ let $t_H = \tau(p_1)$. There is a head wave and its arrival time is $t_H$. Let us write (6) in the form

$$u(t) = \int_{\tau(0)}^{t} U(\tau)\, d\tau \tag{B.7}$$

where $U(\tau)$ is $2/\pi$ times the imaginary part of the integrand in (B.6). We carry out the evaluation of (B.7) as follows:

$$\left.\begin{aligned}
&p_1 \geqslant p_0; \\
&\qquad u(t) = 0, \qquad t \leqslant t_0 \\
&\qquad u(t) = \int_{t_0}^{t} U(\tau)\, d\tau, \; t > t_0, \; p \text{ complex} \\
&p_1 < p_0; \\
&\qquad u(t) = 0 \qquad t \leqslant t_H \\
&\qquad u(t) = \int_{t_H}^{t} U(\tau)\, d\tau, \; t_H < t \leqslant t_0, \; p \text{ real} \\
&\qquad u(t) = \int_{t_H}^{t_0} U(\tau)\, d\tau + \int_{t_0}^{t} U(\tau)\, d\tau, \; t > t_0.
\end{aligned}\right\} \tag{B·8}$$

In the last of (B.8) $p$ is real for $\tau < t_0$ and complex for $\tau > t_0$. The separation of $u(t)$ into the part corresponding to the head wave and the part corresponding to the reflection facilitates the interpretation and the evaluation of (B.6).

The evaluation of the integral in (B.6) is a relatively simple problem in numerical analysis, but all of the calculations in the main text were made using the approximations in Appendix A. This amounts to using the first term in the asymptotic approximation of $K_n(spR)$ for large argument. Knopoff & Gilbert (1959) have shown that such an approximation gives the correct first motion even for $R = 0$. For pulses as short as those calculated in this paper it is a valid approximation to use. However, calculations for long period body waves should be made with integrals typified by (B.6).